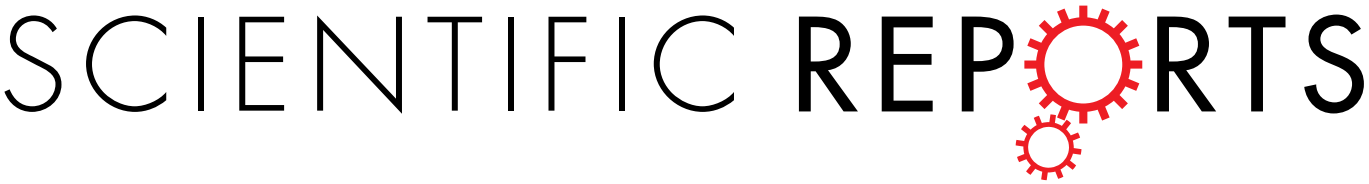

OPEN

Synthesis of Reduced Grapheme Oxide as A Platform for loading β-$NaYF_4$:Ho^{3+}@TiO_2Based on An Advanced Visible Light-Driven Photocatalyst

Received: 3 August 2016
Accepted: 29 September 2017
Published online: 23 October 2017

Zihong Fan[1], Tianhui Wu[2] & Xuan Xu[2]

In this paper a novel visible light-driven ternary compound photocatalyst (β-$NaYF_4$:Ho^{3+}@TiO_2-rGO) was synthesized using a three-step approach. This photocatalyst was characterized using X-ray diffraction, Raman scattering spectroscopy, scanning electron microscopy, energy-dispersive X-ray spectroscopy, Transmission electron microscopy, X-ray photoelectron spectroscopy, fluorescence spectrometries, ultraviolet-visible diffuse reflectance spectroscopy, Brunauer–Emmett–Teller surface area measurement, electron spin resonance, three-dimensional fluorescence spectroscopy, and photoelectrochemical properties. Such proposed photocatalyst can absorb 450 nm visible light while emit 290 nm ultraviolet light, so as to realize the visible light-driven photocatalysis of TiO_2. In addition, as this tenary compound photocatalyst enjoys effecitve capacity of charge separation, superior durability, and sound adsorb ability of RhB, it can lead to the red shift of wavelength of absorbed light. This novel tenary photocatalyst can reach decomposition rate of RhB as high as 92% after 10 h of irradiation by visible-light Xe lamp. Compared with the blank experiment, the efficiency was significantly improved. Recycle experiments showed that theβ-$NaYF_4$:Ho^{3+}@TiO_2-rGOcomposites still presented significant photocatalytic activity after four successive cycles. Finally, we investigated visible-light-responsive photocatalytic mechanism of the β-$NaYF_4$:Ho^{3+}@TiO_2-rGO composites. It is of great significance to design an effective solar light-driven photocatalysis in promoting environmental protection.

Semiconductor photocatalysis has attracted worldwide attention due to its potential inresolving the energy and environmental-related problems through increasing solar energy conversion[1,2]. Titanium dioxide (TiO_2), as one of the most promising photocatalysts, has been widely adopted for degrading inorganic and organic pollutants because of its strong oxidizing capacity under ultraviolet (UV) light, extraordinary chemical stability, sound biocompatibilty and environmental friendliness[3–6]. However, due to the wide bandgap of TiO_2 (Eg = 3.0–3.2 eV), only the UV light with wavelength less than 387 nm, which accounts for ca. 5% of total solar energy, could produce effective photocatalytic activity[7]. While the visible light (Vis) and near-infrared (NIR), which account for ca. 48% and ca. 45%, respectively, are not valid for photocatalysis[8]. Furthermore, the fast recombination of charge carriers will significantly reduce the catalytic activity in practical applications[9,10]. As a result, further innovative researches are needed to realize large scale practical application of TiO_2-based photocatalysts for solving environmental and energy problems.

To resolve this problem, many attempts have been made to improve the photocatalytic activity of TiO_2 by inhibiting the recombination of photogenerated electron–hole pairs and extending the absorption range of TiO_2 towards Vis region, so as to realize a better use of solar energy[11–13]. For example, to extend the bandgap of TiO_2 towards Vis, conventional methods such as introduction of metals[14] or nonmetals[15], surface modification[16], and

[1]Chongqing Key Laboratory of Catalysis and Functional Organic Molecules, College of Environmental and Resources, Chongqing Technology and Business University, Chongqing, 400067, China. [2]Key Laboratory of Three Gorges Reservoir Region's Eco-Environment, Ministry of Education, Chongqing University, Chongqing, 400045, China. Correspondence and requests for materials should be addressed to X.X. (email: xuxuan@cqu.edu.cn)

structure optimization[17] have been used to extend the bandgap of TiO_2 toward Vis energies. In these processes, noble metal doping, composite semiconductor, and holes scavenger can effectively inhibit the recombination of electrons and holes. Although these methods can extend the absorption of TiO_2 to the Vis region and inhibit the recombination of photogenerated electron–hole pairs, many new defects may occur when adjusting the internal lattice and band structure to shorten the bandgap of TiO_2 and let the electrons pass quickly[18]. For instance, with the implementation of these methods, it will cause decreased stability and service life of TiO_2, as well as low activity under UV light[19,20]. Thus, other methods must be sought to extend the absorption range of TiO_2 and thus to enhance the photocatalysis activity.

Recently, lanthanide-doped upconversion (UC) nanophosphors have attracted tremendous interest because of their narrow emission bands, long luminescence lifetime, as well as their physicochemical properties that are conductive to extending the absorption range of TiO_2 edge up to the Vis region or even to the NIR region by UC luminescence of rare earths[21–24]. In order to efficiently utilize the valuable UC energy transferred from the excited UC core, a coupling model was proposed to increase the luminous efficiency, of which the core-shell structure has potential in protecting the UC core from surface quenching and in increasing the efficiency of transferring energy to the photocatalyst shell[25–28]. For examples, the preparation of (α, β)-$NaYF_4$:Yb^{3+},Tm^{3+}@TiO_2, YF_3:Yb^{3+},Tm^{3+}@TiO_2, and Y_2O_3:Yb^{3+} has been reported, wherein the core-shell composite of UC@TiO_2can emit UV and Vis and show an effective photocatalysis under NIR light[29–33]. However, Yb^{3+}, an important sensitizer, has only one excitation at 980 nm in the NIR region. Its UC efficiency is limited by NIR radiation source excitation, which is mainly due to its extremely weak absorption in the NIR wavelength range[34]. We conducted researches on core-shell microcrystal of β-$NaYF_4$:Ho^{3+}@TiO_2 and on the use of Vis as a photocatalyst[35]. This combination takes advantages of Vis and NIR which accounts for ca. 48% and 45% of total solar energy, respectively. However, there still remains some problems about core–shell structure of UC@TiO_2.For example, the efficient utilization of light is limited, because the light cannot penetrate the cores of UC nanocrystals. Moreover, the fast recombination of photogenerated electron–hole pairs of UC@TiO_2should not be ignored as they can affect the photocatalytic efficiency[36]. Therefore, it is needed to seek other methods to solve these problems.

Graphene (GR) and reduced graphene oxide (rGO) have emerged as attractive candidates for constructing GR–based materials because of their several valuable characteristics[37–40]. First, GR materials exhibit high electron mobility (200, 000 cm^2/V) and extended π-electron conjugation, therefore GR is a good material for transporting electrons and stabilizing extraneous electrons. In addition, GR enjoys high specific surface area (2630 m^2/g) and unique flexible sheet-like structure. Recently, great attention has been attracted by TiO_2–GR, which displays the capacity of significantly improving photoelectrochemical catalytic activity[41,42]. As of now, there have been lots of reports on TiO_2–GR composites. Researches indicate that GR can not only increase the adsorption surface of the catalyst because of its high theoretical specific surface area, but also can improve the adsorption performance of TiO_2 by chemical adsorption[42]. The TiO_2@GR composite has high light transmittance and zero-bandgap of GR. Moreover due to the excellent electrical conductivity for electrons storing and shuttling (flexible sheet-like structure), it can inhibit the recombination of photogenerated electron–hole pairs[43–48]. Moreover, the formation of Ti–O–C bonds can expand the light absorption to longer wavelengths[49]. After absorbing photons on the surface of GR, the electrons are injected into the TiO_2 conduction band to form a reactive exciton (·OH, O_2^-) for degradation of organic pollutants. Despite all the advantages, these TiO_2@GR composites are subjected to a low-usage of natural sunlight, which will limit the photocatalytic activity under solar irradiation[50].

In general, there are at least two major challenges which may lead to the difficulty in realizing the large scale practical application of TiO_2 photocatalysis. One is how to improve the utilization rate of solar light, which can be realized through extending the absorption range of TiO_2 using UC nanophosphors[36,51,52]. The other one is how to inhibit the recombination of photogenerated electron–hole pairs. The GR/rGO is expected to serve as an electron collector and transporter, which can accept and shuttle the electrons generated from the semiconductors, and thus preventing recombination and prolonging lifetime of the photogenerated electron–hole pairs. A series of studies have been carried out in these two aspects. Long and Wang[36,52] studied on the preparation of YF_3:Yb^{3+},Tm^{3+}/P25/GR and α-$NaYF_4$:Yb^{3+},Tm^{3+}/TiO_2/rGO composites that emit UV and Vis light under 980 nm excitation and show a higher efficiency as compared with a physical mixture. Nevertheless, following questions are still existed. Firstly, the individual components (i.e. UC materials, P25–TiO_2 and GR) are only physically mixed without well-defined nanostructures. Secondly, the nanosized YF_3 and α-$NaYF_4$ have relatively low UC abilities compared with the microsized hexagonal phase (β-$NaYF_4$)[53]. So the technology can still be improved. Wang *et al.*[51] studied on the preparation of β-$NaYF_4$:Yb^{3+}, Tm^{3+}/N-P25/GR composites as an advanced NIR and Vis-driven UC photocatalyst. However, the individual components are only physically mixed without well-defined nanostructures. As a result, the photocatalytic activity under NIR is relatively low and unsatisfactory. Meanwhile, the existing researches are mainly focused on the sensitization agent. Yb^{3+}, an important sensitizer, has only one excited electronic state around the near-infrared region (980 nm). Therefore, the excitation sources for Yb^{3+}-doped UC materials are in the near-infrared range, rather than in the Vis range. It is difficult to convert near-infrared radiation to higher energy UV radiation, because the UC process requires the absorption of three photons or more. As a result of this requirement, UC efficiency of Yb^{3+}-doped UC materials is low when a near-infrared radiation source is used. However Ho^{3+} single-doped UC materials have received little attention, and studies have indicated that Ho^{3+} single-doped UC nanoparticles can absorb Vis light and emit UV radiation. This combination also takes advantage of the Vis light which accounts for ca. 48% of total solar energy.

In this paper, we integrated the above-mentioned strategies and demonstrated the rGO–assisted core–shell structure β-$NaYF_4$:Ho^{3+}@TiO_2 could act as a new Vis-driven photocatalyst for the first time. Benefiting from the high specific surface area and the flexible sheet-like structure, rGO emerged as an excellent platform on which the core–shell microcrystal β-$NaYF_4$:Ho^{3+}@TiO_2 can be load to form the ternary composite β-$NaYF_4$:Ho^{3+}@TiO_2–rGO. In this photocatalyst, it is expected to emit UV light after absorbing Vis light of the solar spectrum during the loading process of UC microcrystals, meanwhile the optical response of the β-$NaYF_4$:Ho^{3+}@TiO_2–rGO will

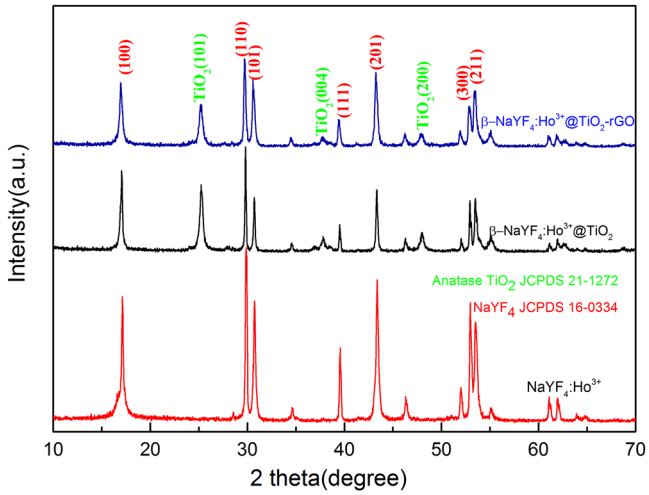

Figure 1. The XRD patterns of β-$NaYF_4$:Ho^{3+}, β-$NaYF_4$:Ho^{3+}@TiO_2, and β-$NaYF_4$:Ho^{3+}@TiO_2-rGO.

be enhanced from UV to Vis. In addition to the microcrystals catalyst β-$NaYF_4$:Ho^{3+}@TiO_2–rGO which can improve the utilization of sunlight, rGO can inhibit the recombination of photogenerated electron–hole pairs and enhance the adsorption capacity of the photocatalyst. In addition, we conducted detailed discussion on the Vis responsive photocatalytic mechanism of β-$NaYF_4$:Ho^{3+}@TiO_2–rGO.

Results and Discussion

Structure and morphology characterizations. Figure 1 shows the XRD patterns of β-$NaYF_4$:Ho^{3+}, β-$NaYF_4$:Ho^{3+}@TiO_2 and β-$NaYF_4$:Ho^{3+}@TiO_2-rGO, respectively. From the XRD images of the three samples in Figure. 1, we can see that diffraction peaks are very sharp. This indicates that the samples resulted from hydrothermal synthesis are of high purity and excellent crystallinity, and such excellent crystallinity plays a vital role in determmining the photocatalysis efficiencies[54]. In addition, we can see that the diffraction peaks of UC material at 17.2°, 30.1°, 30.8°, 43.5°, and 53.7° can perfectly match with the standard card of β-$NaYF_4$(JCPDS no. 16–0334), without the occurrence of impurity-contained diffraction peak. This indicates that the high purity UC material β-$NaYF_4$ prepared using hydrothermal method is the current well-recognized substrate of the highest luminous efficiency[53]. Through comparing with standard card, it can find the compound material β-$NaYF_4$:Ho^{3+}@TiO_2 not only involved all diffraction peaks of β-$NaYF_4$, but also showed the characteristic diffraction peak of TiO_2 when $2\theta = 25.4°$, which was consistent with anatase standard card (JCPDS no. 21–1272). Therefore, it proved that the TiO_2 included in photocatalyst prepared by sol-gel method was anatase-typed TiO_2, which enjoyed higher photocatalysis effect than rutile type TiO_2 and was more helpful in increasing the photocatalysis activity of the compound material[55]. Moreover, β-$NaYF_4$:Ho^{3+}@TiO_2 prepared by such method will not change the crystal form of β-$NaYF_4$, therefore it can be known such method has sound stability and reproducibility. Through comparing the XRD pattern between β-$NaYF_4$:Ho^{3+}@TiO_2-rGO and the compound material, it can observe no occurrence of new peak value, and all peak values are either hexagonal hexagonal or anatase-typed TiO_2. It can also be noted that the diffraction peak of rGO is not reflected in such XRD pattern, which we think may be due to its low proportion in compound material and its low concentration that is under the LOD of XRD. Therefore, other characterization methods are still needed to verify the existence of rGO.

In addition, it is worth noting that it can observe no diffraction peaks of Ho^{3+} from UC material, compound material, or ternary complex in above figure, which is either because Ho is not successfully doped in, or because it is exsited in other forms. The existence form of Ho is of vital significance to UC luminousmechanism, therefore it is needed to seek other characterization methods.

To determine the micromorphologies and the presence of rGO these samples, we conducted SEM and TEM characterization for β-$NaYF_4$:Ho^{3+}, β-$NaYF_4$:Ho^{3+}@TiO_2, andβ-$NaYF_4$:Ho^{3+}@TiO_2-rGO, respectively, and the results are shown in Figure. 2. From Figure. 2a,b, it can be seen that the prepared UC materials are hexagonal prisms in uniform sizes, regular shapes, and with smooth surfaces. These hexagonal microcrystals have lengths of around 8 um and diameters of nearly 2.4 um, which is consistent with XRD characterization result. There is a close correlation between UC luminous efficiency and host material size. The larger the host material size is, the higher the luminous efficiency will be[56]. This indicates that the UC host material prepared by hydrothermal method is of sound luminous efficiency. After being compounded with TiO_2 shell by sol-gel method, the UC material had not changed very much on its morphology, but still remain in shape of hexagonal prism. After coating, the surfaces become coarser (Figure. 2c), showing that the microcrystals are successfully coated with a TiO_2 layer. The β-$NaYF_4$:Ho^{3+} microcrystals are equably coated by the TiO_2 shell. For further detailed structure analysis, the characterization of the β-$NaYF_4$:Ho^{3+}@TiO_2 core-shell microcrystals was carried out by TEM. Figure 2d show enlarged image in which the β-$NaYF_4$:Ho^{3+}@TiO_2 core-shell structure is clearly seen; the core of β-$NaYF_4$:Ho^{3+} exhibits a dark color. These images confirm that the UC microcrystals are uniformly coated by a TiO_2 layer. The average thickness of the TiO_2 shells is about 50 nm. Core-shell structure model is beneficial to realizing high efficient energy transfer between UC material and photocatalyst. The SEM image of ternary

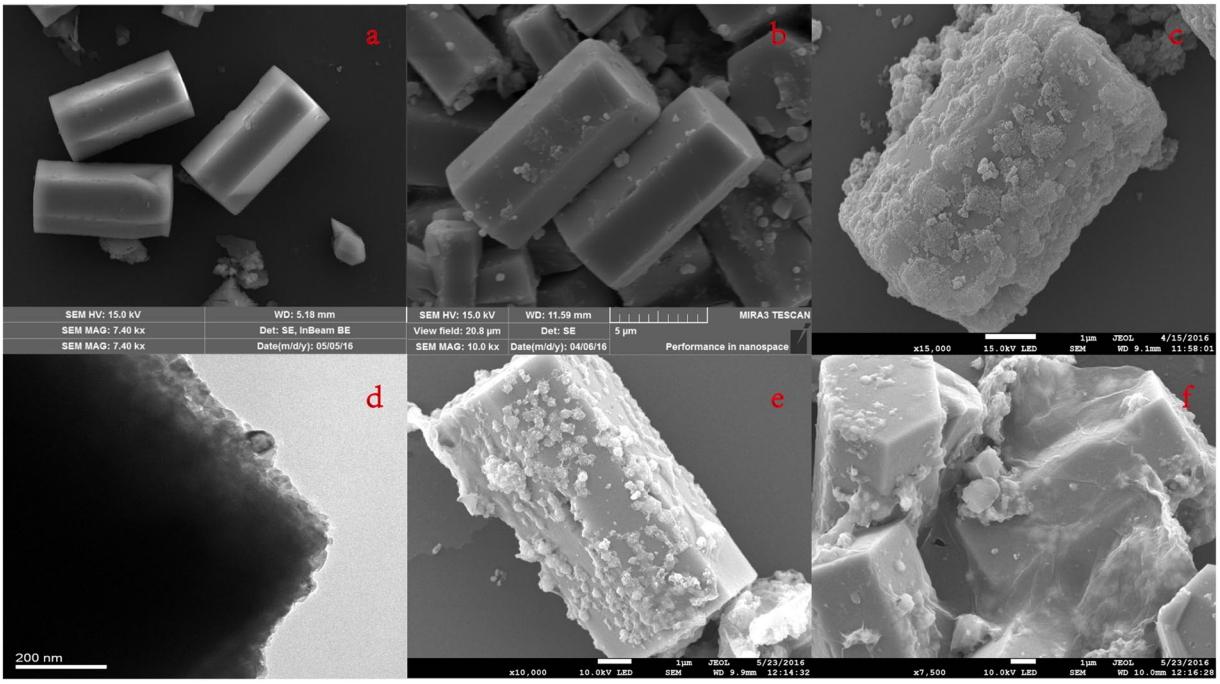

Figure 2. SEM images of (**a**,**b**) β-$NaYF_4$:Ho^{3+}, (**c**) β-$NaYF_4$:Ho^{3+}@TiO_2, and (**e**,**f**) β-$NaYF_4$:Ho^{3+}@TiO_2–rGO, (**d**) TEM images ofβ-$NaYF_4$:Ho^{3+}@TiO_2.

complex β-$NaYF_4$:Ho^{3+}@TiO_2-rGO in Figure. 2e,f shows that there are massive amounts of rGO lamellas deposited on the surface of compound material. There are small amount of deciduous TiO_2 existing on the surfaces of some rGO lamellas; some rGO serve as substrates, on which compound materials are loaded; some rGO serve as carriers, which wrap the compound materials; The coupling between rGO and β-$NaYF_4$:Ho^{3+}@TiO_2 is positive to the high efficient transferring of charge, and thus increasing the separation efficiency of photongenerated carriers.

Composition and chemical states. Energy dispersive X-ray spectroscopy (EDS) was conducted to determine the element composition of β-$NaYF_4$:Ho^{3+}@TiO_2-rGO and to further confirm the successful doping of Ho element. Results are shown in Figure. 3. According to the scan results of EDS surface of ternary compound material in Figure. 3b–h, it can observe the existences of Y, F, Na, Ho, Ti, O and C in ternary compound material β-$NaYF_4$:Ho^{3+}@TiO_2-rGO, wherein C element is in homogeneous distribution, which indicates a sound dispersion effect of rGO. Figure 3i presents the mass percent of each element. However, EDS can only characterize the existence of in prepared sample, rather than charaterizing the existence form of Ho.

XPS characterization method was used to determine the chemical states of elements on the surface of β-$NaYF_4$:Ho^{3+}@TiO_2-rGO as shown in Figure. 4. According to the full spectrum image in Figure. 4a, it shows that such sample contains Ti, O, Na, Y, F, Ho and C elements. C 1 s peak (284.1 eV) is the spectrum internal reference. Figure 4b shows that the Ti2p photoemission peak of compound material consists of two sub-peaks, with binding energies of 458.3 eV and 464.1 eV, corresponds to Ti $2p_{3/2}$ and Ti $2p_{1/2}$, respectively, which is consistent with the XPS spectrum of TiO_2 as described[57]. As shown by the O1s in Figure. 4c, there is at least one type of oxygen in the compound material. The binding energies of two peaks are 529.9 eV and 532.3 eV, which are corresponded to the characteristics of Ti–O–Ti and H–O, respectively. The element F displays one characteristic peak at 684.3 eV because of the core level of F1s (see Figure. 4d). The C1s XPS spectrum shows two characteristic peaks, corresponding to oxygenated ring C bonds (284.7 eV for C-C, C=C and C-H,286.2 eV for C-O, and 288.6 eV for the C=O bond). These results indicate that there exist abundant oxygen-containing functional groups onrGO surface. However, in the C 1 s XPS spectra of β-$NaYF_4$:Ho^{3+}@TiO_2-rGOas shown in Fig. 4e, the relative intensities of the three components associated with C-O/C=O bonds decrease significantly, indicating that some of the oxygen functional groups were reduced during the chemical reduction process[58,59]. Doped elements can also be detected by XPS. Figure 4f represents the characteristic peak of Ho^{3+} at binding energy of 159.5 eV and 161.1 eV, respectively. XPS characterization results show that the Ho element in the sample exists in the form of Ho^{3+} and has been successfully doped into the crystal lattice of the host material β-$NaYF_4$.

To further confirm the reduction of GO, we conducted FTIR analysis for the samples, and the results are shown in Figure. 5. It shows that GO contains abundant oxygen containing functional groups. The strong peak occurred at 1731 cm^{-1} is mainly caused by the tensile vibration of C=O in carboxyl functional groups, while the strong peak at around 1623 cm^{-1} is mainly caused due to the lack of oxidized C=C structure in graphite structure. In addition, the occurrence of peak at 1401 cm^{-1} is due to the oxidized C-OH on the surface. The occurrences of peaks at 3405 cm^{-1} and 1048 cm^{-1} are due to the vibrations of OH and C-O[60], respectively. Through comparing β-$NaYF_4$:Ho^{3+}@TiO_2-rGO and GO, it can find that C-O and C=O, at 1084 cm^{-1} and 1731 cm^{-1} respectively, are

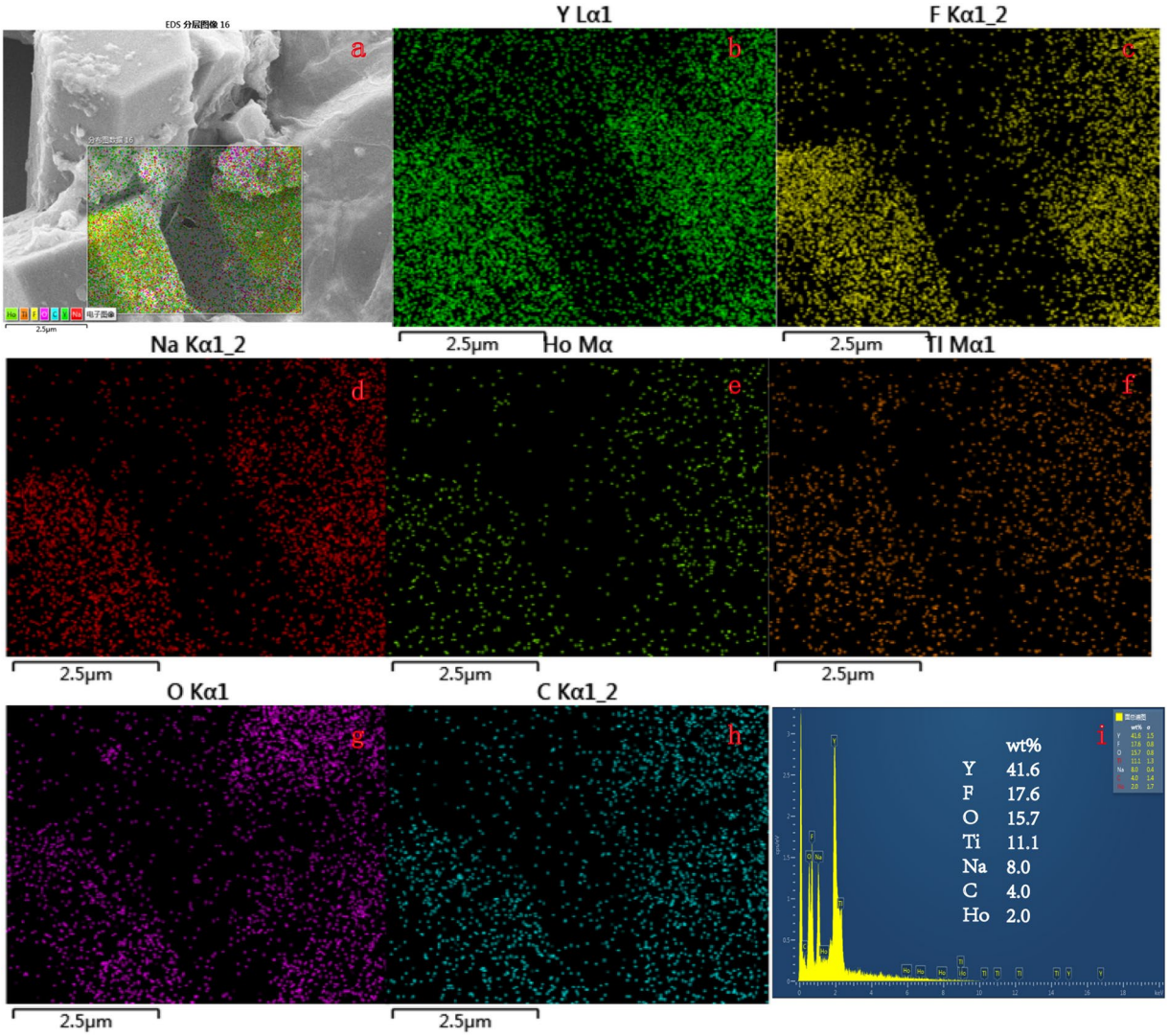

Figure 3. (**a**) SEM images ofβ-$NaYF_4$:Ho^{3+}@TiO_2–rGO, (**b**–**h**) SEM elemental distribution mappings of Y, F, Na, Ho, Ti, O, and C. (**i**) EDS spectrum of β-$NaYF_4$:Ho^{3+}@TiO_2–rGO.

almost disappeared, which indicates that some carboxy groups are differentially reduced according to different conditions. The functional groups at 1623 cm^{-1} and 1401 cm^{-1} are also significantly reduced. Results show that the GO can be effectively reduced into rGO using hydrothermal method, which is consistent with XPS result. β-$NaYF_4$:Ho^{3+}@TiO_2-rGO displays a strong and wide absorption peak, which is proved to be a combination peak caused by the stretching vibration of Ti-O-Ti and Ti-O-C[61]. Moreover the existence of Ti-O-C bond indicates existence of chemical bond force between rGO and TiO_2, and such chemical bond is beneficial to the red shift of absorbed wavelength[49], so as to better take the advantage of solar photocatalysis.

Photoluminescence properties. Figure 6a shows the UV-Vis diffuse reflection spectrum of ternary compound material β-$NaYF_4$:Ho^{3+}@TiO_2-rGO. Results show that the UV-Vis diffuse reflection spectrum of β-$NaYF_4$:Ho^{3+}@TiO_2-rGO has two distinguished features as compared with β-$NaYF_4$:Ho^{3+}@TiO_2, β-$NaYF_4$:Ho^{3+}, β-$NaYF_4$, and P25, wherein one is the overall improvement of Vis light absorption property, and the other one is the red shift of absorption cross section. Both features are positive to increasing the photocatalytic activity[7]. In addition, we observed that β-$NaYF_4$:Ho^{3+} displayed three weak absorption peaks at 450 nm, 537 nm, and 642 nm, respectively, while β-$NaYF_4$ did not show absorption peak. This indicates the UC material excited ion Ho^{3+} is of vital significance to luminescence. On the whole, the absorption peak at 450 nm is relatively stronger. As we know that the stronger the light-absorbing capacity of the absorption peak is, the more suitable the absorption peak will be serving as excitation wavelength. Therefore the absorption peak at 450 nm was finally selected as the excitation wavelength for the luminescence spectrum of UC material β-$NaYF_4$:Ho^{3+}.In the absorption spectrum of GO, it shows the absorption peaks of GO at 230 nm (π-π* transitions of C=C bonds)[62] referred to pure GO films shown in Figure. 6a. rGO has a characteristic absorption peak at 270 nm, compared with GO 40 nm red shift of absorption spectrum, the overall absorption intensity increases, indicating that GO in hydrothermal conditions reduction. The carbon atoms of sp^3 hybridized into sp^2 hybrid structure, improved GR

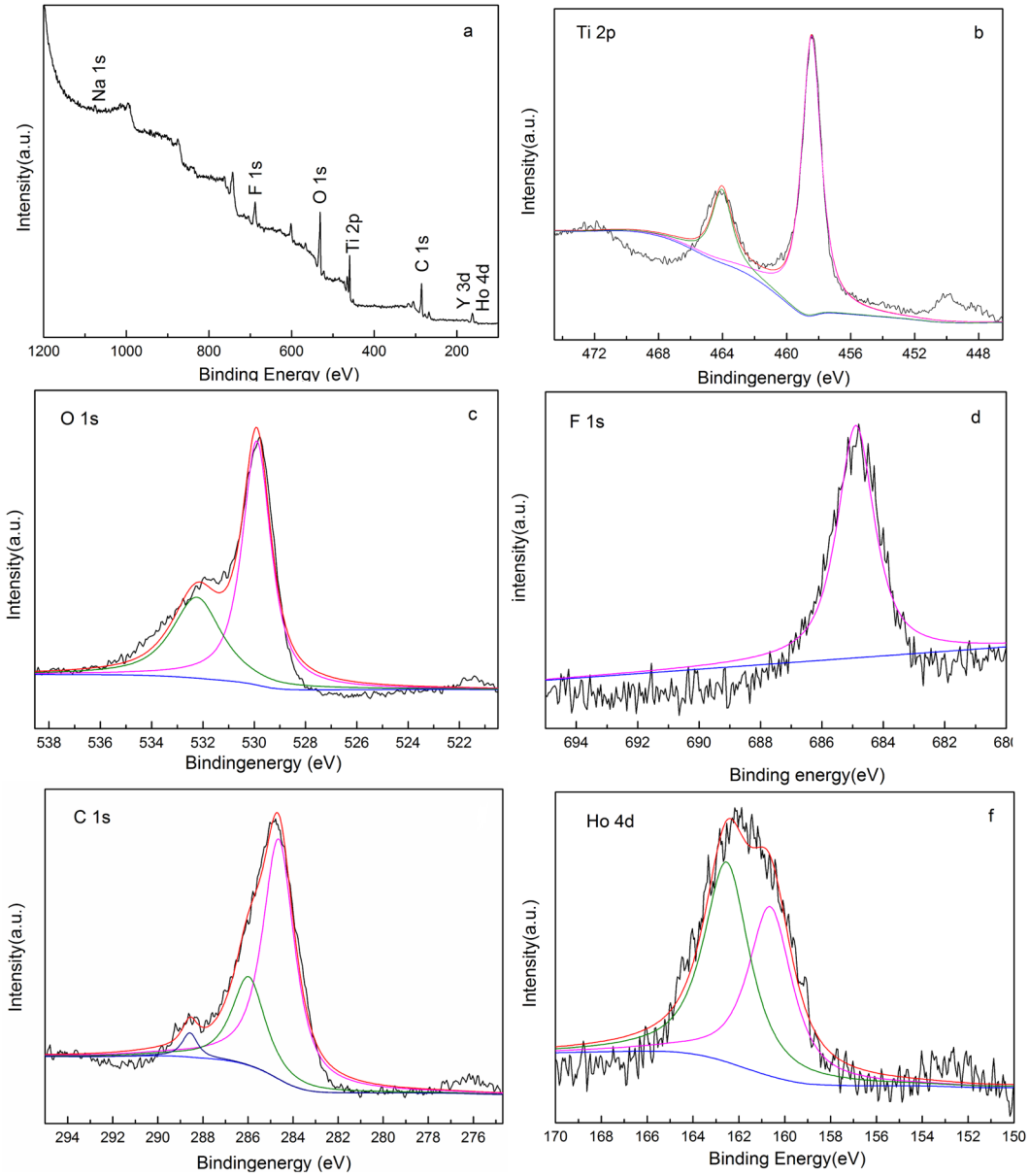

Figure 4. High-resolution XPS analyses of the β-$NaYF_4$:Ho^{3+}@TiO_2-rGO microcrystals: (**a**) Wide spectrum, (**b**) Ti 2p, (**c**) O 1 s, (**d**) F 1 s, (**e**)C 1 s, (**f**) Ho 4d.

was largeπelectron conjugated structure[63]. sUV-Vis characterization results show that the rGO was successfully prepared by hydrothermal synthesis.

The bandgaps of P25, β-$NaYF_4$:Ho^{3+}@TiO_2, and β-$NaYF_4$:Ho^{3+}@TiO_2-rGO can be calculated using Tauc's formula, and the calculation results are shown in Figure. 6b. The bandgap of P25 is 3.20 eV (387.5 nm), the bandgap of β-$NaYF_4$:Ho^{3+}@TiO_2 is 3.18 eV (389.9 nm), and the bandgap of β-$NaYF_4$:Ho^{3+}@TiO_2-rGO is 3.09 eV (401.3 nm). From the results, it can conclude that the UC materialβ-$NaYF_4$:Ho^{3+} microcrystal is of limited influence to the bandgap of TiO_2, while the introduced rGO is of larger influence to its absorption cross section, such as reducing its bandgap and leading to the red shift of absorbed wavelength. From Figure. 6c, it can be seen that the VB edges ofβ-$NaYF_4$:Ho^{3+}@TiO_2 are estimated to be 0.32 eV. According to the bandgap and the valence band (VB) position of the samples, we can draw the bandgap structures as displayed in Figure. 6c inset, from which it can be clearly seen that the conduction band (CB) and VB position of β-$NaYF_4$:Ho^{3+}@TiO_2.

Figure 6d shows the UC Luminescence spectra of β-$NaYF_4$:Ho^{3+}, β-$NaYF_4$:Ho^{3+}@TiO_2, and β-$NaYF_4$:Ho^{3+}@TiO_2-rGO respectively under 450 nm excitation. It can be seen that under 450 nm excitation, there is a emission peak at 290 nm in ultraviolet region, which corresponds to the radiative transition of Ho^{3+} from $^5D_4$ to $^5I_8$. After being doped with TiO_2, the emission peak wavelength location of composite material of β-$NaYF_4$:Ho^{3+} has not been changed, which indicates that the UC luminance properties remain unchanged after compounded with TiO_2. In addition, we can observe that β-NaYF4:Ho^{3+}@TiO_2 shows a fairly weak luminous intensity at 290 nm under the 450 nm excitation, wherein the emission peak is almost disappeared. This may be because the UV-light

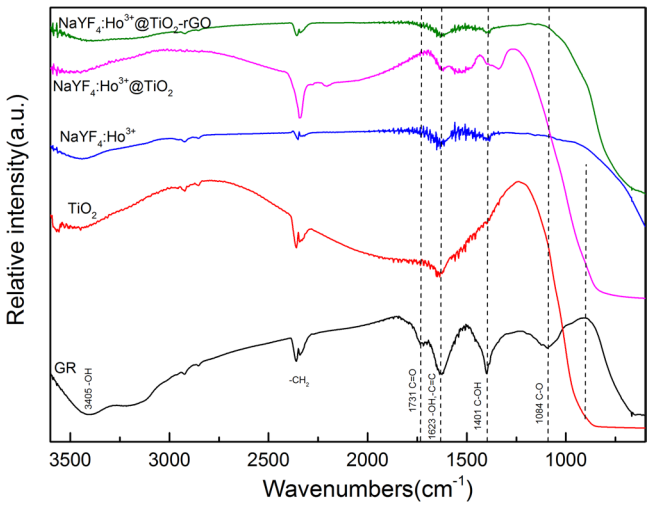

Figure 5. FTIR spectra of GO, TiO_2, β-$NaYF_4$:Ho^{3+}, β-$NaYF_4$:Ho^{3+}@TiO_2, and β-$NaYF_4$:Ho^{3+}@TiO_2-rGO, respectively.

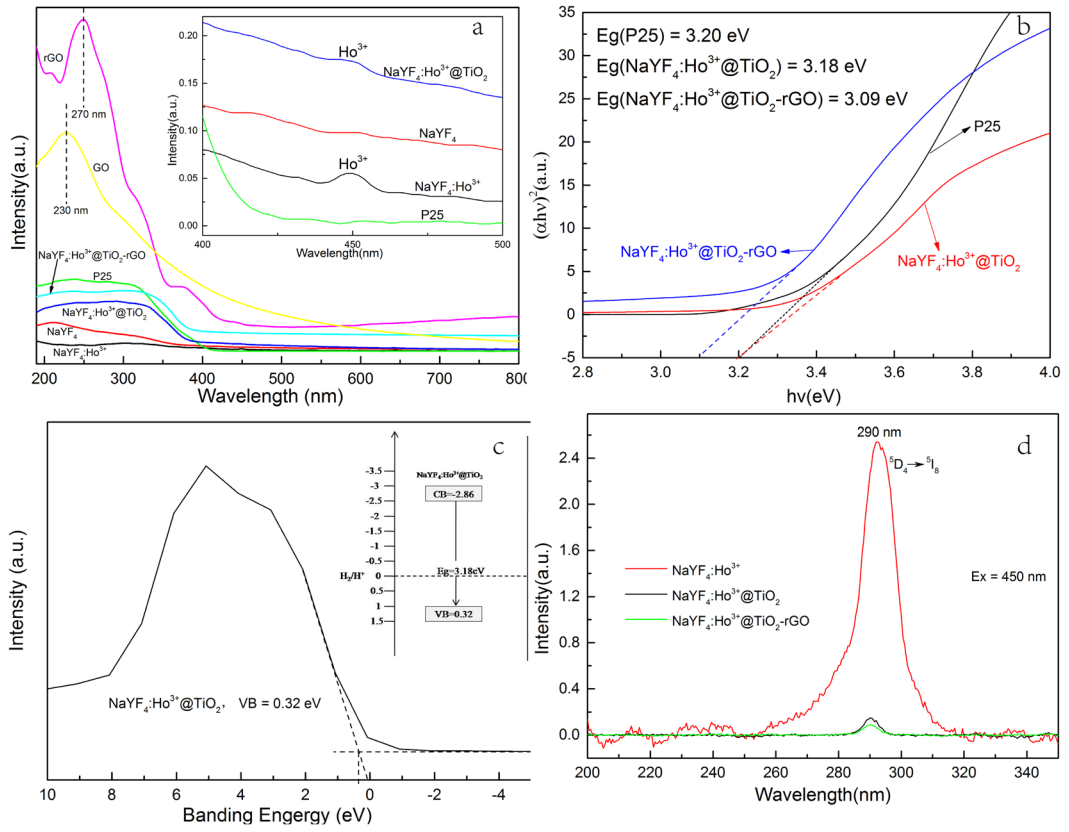

Figure 6. (**a**) The UV-Vis absorbance spectra of the P25, β-$NaYF_4$, β-$NaYF_4$:Ho^{3+}, β-$NaYF_4$:Ho^{3+}@TiO, β-$NaYF_4$:Ho^{3+}@TiO_2-rGO, GO, and the RGO prepared by hydrothermal method under the same conditions asβ-$NaYF_4$:Ho^{3+}@TiO_2-rGO; inset: the enlarged spectra ranging from 400 nm to 500 nm. (**b**) The plot for bandgap energy Eg. (**c**) VB XPS; inset: schematic illustration of the band gap structures. (**d**) Photoluminescence (PL) spectra of samples under 450 nm excitations.

emitted from β-$NaYF_4$:$Ho^{3+}$was absorbed by the TiO_2 wrapped on the surface, so that the phenomenon of photocatalysis is resulted. As it is well known that rGO is an effective material which is of high ability in absorbing light[64]. For rGO-assisted β-$NaYF_4$:Ho^{3+}@TiO_2, there were less light emitted from the system, while more irradiated lights were absorbed in. It is reasonable that stronger irradiated light will induce higher intensity of the

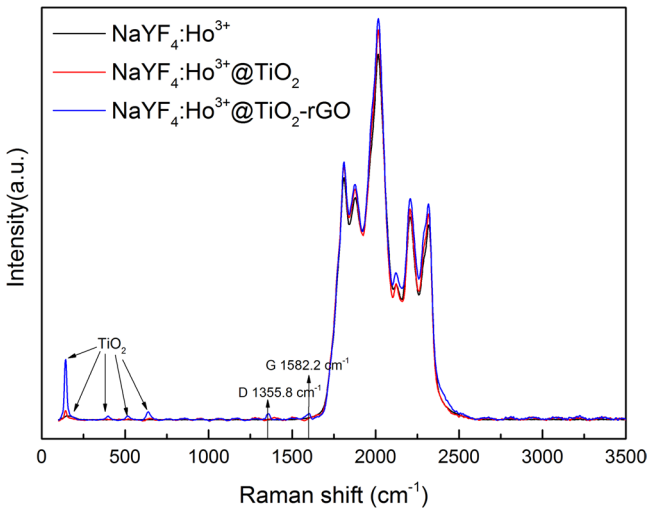

Figure 7. Raman spectra of $NaYF_4:Ho^{3+}$, $NaYF_4:Ho^{3+}@TiO_2$, and $NaYF_4:Ho^{3+}@TiO_2$-rGO composite.

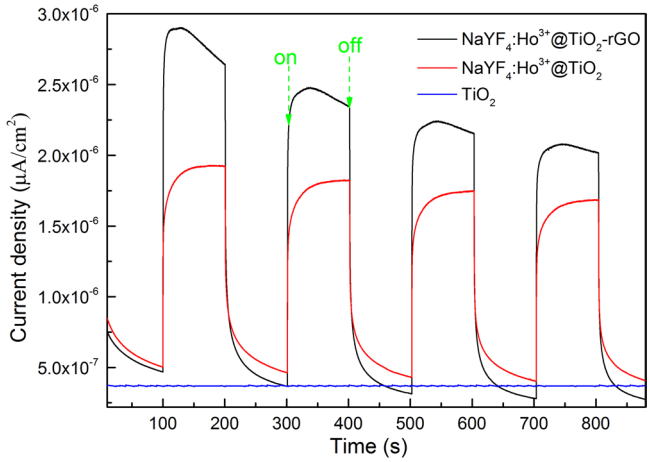

Figure 8. Transient photocurrent densities of the as-prepared samples.

converted light. Hence, the low emission intensity detected here can be ascribed to the fact that most of the converted lights were absorbed by the composite with the help of rGO.

Ramna spectra. The Raman spectra of $NaYF_4:Ho^{3+}$, $NaYF_4:Ho^{3+}@TiO_2$, and $NaYF_4:Ho^{3+}@TiO_2$-rGO composite are presented in Figure. 7. The Raman spectrum of rGO displayed two prominent peaks at 1355.8 and 1582.2 cm^{-1}, corresponding to the well-documented D and G bands, respectively[65]. G band is Raman active for sp^2 hybridized carbon-based material, while D band is activated only if defects participate the double resonance Raman scattering near K point of Brillouin zone[63]. The specific vibration modes are located around 140, 399, 517, and 639 cm^{-1}, indicating the presence of the anatase phase in all of these samples[66]. The intensity ratio of D band to G band (I_D/I_G) is correlative with the average size of sp^2 domains[67]. Higher I_D/I_G ratio means the smaller size of sp^2 domains. From Figure. 6, the I_D/I_G ratios for $NaYF_4:Ho^{3+}@TiO_2$-rGO were1.04, further confirmation the$NaYF_4:Ho^{3+}@TiO_2$-rGO composite further confirmed the formation of rGO sheets[63]. Raman spectroscopy is one of the most common, rapid, non-destructive and high-resolution techniques for characterizing carbon materials[67]. Previous studies have shown that certain Raman peaks change sensitively with the number of GR layers (n)[68]. This discovery that exhibits Raman fingerprints for single-layer, bilayer, and few-layer GR can be used as identification. The position of the G (1582.2 cm^{-1}) peak of the Raman spectrum was deduced from previous studies that the number of rGO layers was within six layers[67].

Photoelectrochemistry measurements. Photoelectrochemical measurements were performed to investigate the excitation, separation, transfer, and recombination of photoinduced charge carriers[69]. Figure 8 shows the characterization results of photocurrents of electrode TiO_2, β-$NaYF_4:Ho^{3+}@TiO_2$, and β-$NaYF_4:Ho^{3+}@TiO_2$-rGO, based on which it can deduce the electron inteaction between rGO and β-$NaYF_4:Ho^{3+}@TiO_2$. From the Figure. 8 we can see that steady and transient photocurrents can be obtain during the process of cyclically opening and closing Vis light irradiation. Enjoying a large bandgap, the TiO_2 nanoparticle is of no influence to

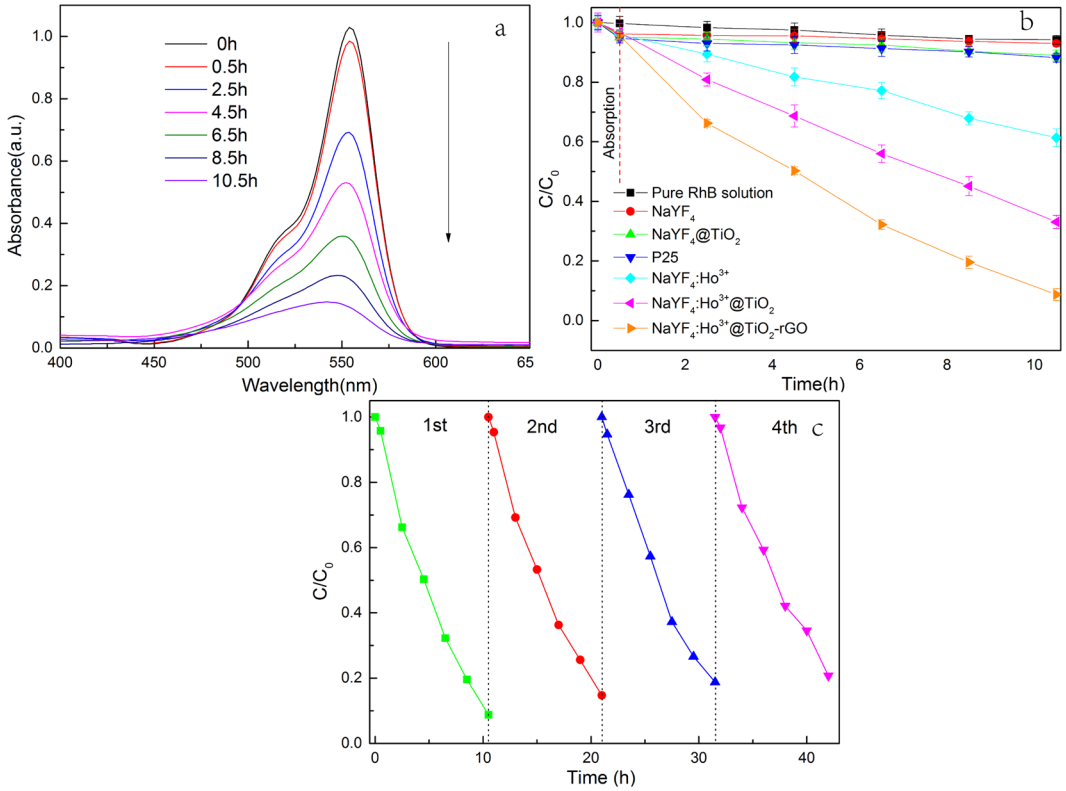

Figure 9. (**a**) Time-dependent UV-Vis absorption spectroscopy of an RhB solution degraded by β-$NaYF_4$:Ho^{3+}@TiO_2-rGO (**b**) Time-dependent plot of the photodegradation of a RhB solution by different catalysts upon irradiation by a Xe lamp (500 W) with a UV cutoff filter (λ > 400 nm). (**c**) Cyclic run of the photocatalytic degradation of RhB using β-$NaYF_4$:Ho^{3+}@TiO_2-rGO.

Vis light, and nearly no photocurrents were resulted. However regarding composite material β-$NaYF_4$:Ho^{3+}@TiO_2, the UC material within first absorbed Vis light and converts it into UV light, and then excited TiO_2 to produce electron-hole pairs, so that photocurrents were produced. It is worth noting that the photocurrent resulted from electrode β-$NaYF_4$:Ho^{3+}@TiO_2-rGO has stronger intensity as compared with photocurrent resulted from β-$NaYF_4$:Ho^{3+}@TiO_2. This is owe to rGO's excellent conductivity that led to the effective separation of electron-hole pairs. The effective separation of electron-hole pairs is a key factor for the enhancement of photocatalysis activity of β-$NaYF_4$:Ho^{3+}@TiO_2-rGO. The results above are consistent with PL analysis results.

Photocatalytic activity and recyclability. Based on RhB as target degradation product, we researched the photocatalytic activity of β-$NaYF_4$:Ho^{3+}@TiO_2-rGO to Vis light. We used 500 Xe lamp coupled with 420 nm cut-off filter as the light source. The time-dependent absorption spectrogram of RhB is shown in Figure. 9a, from which we can see that RhB shows a gradual decreasing absorbance at 554 nm with the extension of time. This indicates β-$NaYF_4$:Ho^{3+}@TiO_2-rGO is of sound degradation effect to RhB under Vis light irradiation.

Figure 9b shows the variation curve of C/C_0 with the increase of optical radiation time, wherein C_0 and C respectively represent the initial concentration of RhB solution and the concentration of RhB after certain period of irradiation time. Results show that photocatalyst β-$NaYF_4$:Ho^{3+}@TiO_2-rGO can reach decomposition rate of RhB as 92% after 10 h of Xe lamp irradiation, which is increased by 25% as compared to the decomposition rate of RhB using β-$NaYF_4$:Ho^{3+}@TiO_2 after 10 h of Xe lamp irradiation. Theβ-$NaYF_4$:Ho^{3+}@TiO_2-rGO exhibited the best photocatalytic efficiency, which was because its larger BET surface area and pore volume (Figure. 10 and Table 1) are beneficial for theβ-$NaYF_4$:Ho^{3+}@TiO_2-rGO composite contacting with organic contaminants, and thus the photocatalytic performance can be enhanced after loading of the rGO sheets. In addition, the rGO facilitated the transport of electrons photogenerated in the TiO_2, and therefore led to efficient separation of photogenerated carriers in the coupledβ-$NaYF_4$:Ho^{3+}@TiO_2-rGO system. Moreover, the photocatalytic degradation of RhB was closely dependent on the Vis light adsorption ability of TiO_2, and the loading of the rGO shortened the bandgap of TiO_2. This explains why there was an increased absorptionof Vis light on TiO_2, and thus why an increased decomposition rate of RhB was resulted in. To eliminate external factors to the degradation effect of phototacatlysis, we conducted a series of comparative tests. We found that the self-decomposition rate of RhB after 10 h of Xe lamp irradiation was only 6%, which indicates the thermal radiation of xenon lamp is of limited influence. By using UV catalyst P25, the decomposition rate of RhB after 10 h of Xe lamp irradiation was only 12%, wherein half of the decomposition rate was ascribed to adsorption degradation. To our surprise, the UC materialβ-$NaYF_4$:Ho^{3+} reached the decomposition rate of RhB as high as 37% after 10 h of Xe lamp irradiation, which was higher than those of β-$NaYF_4$, P25, and β-$NaYF_4$@TiO_2. This is mainly because the non-radiative

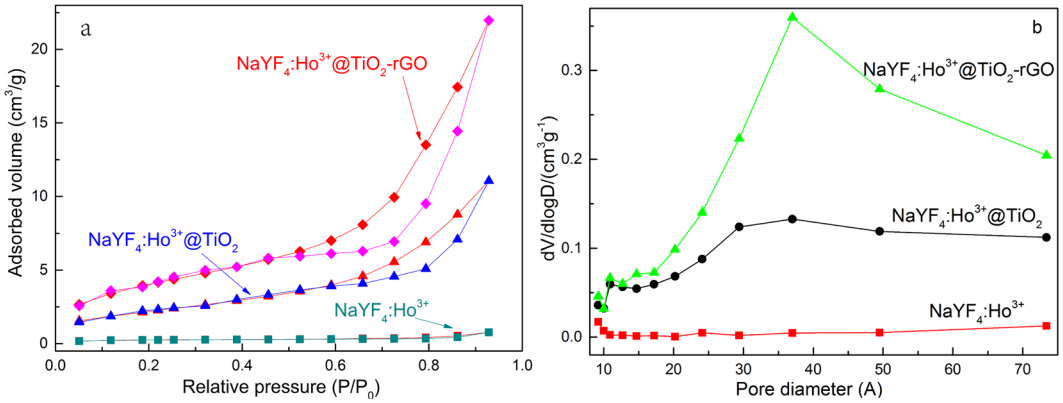

Figure 10. N_2 adsorption-desorption isotherms (**a**) and pore size distribution curves (**b**) of β-$NaYF_4$:Ho^{3+}, β-$NaYF_4$:Ho^{3+}@TiO_2, and β-$NaYF_4$:Ho^{3+}@TiO_2-rGO.

Sample	Mean pore size(nm)	Pore volume(cm^3g^{-1})	Surface area(m^2g^{-1})
$NaYF_4$:Ho^{3+}	3.5123	0.001069	0.8938
$NaYF_4$:Ho^{3+}@TiO_2	3.5915	0.016921	8.3884
$NaYF_4$:Ho^{3+}@TiO_2-rGO	3.9655	0.032805	16.7511

Table 1. Characteristics obtained from nitrogen desorption isotherms.

transition of activator Ho^{3+} in UC material resulted in the UV light of short wavelength (290 nm) which is of higher thermal energy and photosensitization effect, so that RhB can be decomposed more effectively[70]. In addition, due to the absence of doping with Ho^{3+}, the β-$NaYF_4$ and β-$NaYF_4$@TiO_2 after 10 h of Xe lamp irradiation can achieve decomposition rate of RhB as 7% and 11%, respectively, which were far below the levels after doping with Ho^{3+}. This indicates that suitable activator must be selected to induce photon transition before realizing effective UC luminescence.

Photocatalyst should remain unchanged photochemical stability and durability after repeated irradiation, which is of vital significance in practical application. Figure 9c shows the photocatalystic activity of β-$NaYF_4$:Ho^{3+}@TiO_2-rGO after four repeated irradiations. From this figure we can see that after four repeated irradiations, the photocatalytic activity of the sample is insignificantly decreased from 92% to 81% and then tends to be stable. This reveals that the composite photocatalyst is of relatively better stability and reproducibility.

Photocatalyticradical and mechanisms analysis. DMPO-ESR spin trapping spectrum was used to detect ·OH and $\cdot O_2^-$ in solution[71,72]. As shown in Figure. 11a,b, under Vis light irradiation, ·OH and $\cdot O_2^-$ in β-$NaYF_4$:Ho^{3+}@TiO_2-rGO can be successfully detected. Moreover, with the extension of time, the signals of both free radicals are significantly increased, which indicates the accumulation effect of both free radicals as time goes on. To illustrate the influence of the introduction of rGO to the system, we compared the signals of ·OH and $\cdot O_2^-$ of TiO_2, β-$NaYF_4$:Ho^{3+}@TiO_2, and β-$NaYF_4$:Ho^{3+}@TiO_2-rGO at the same time under Vis light irradiation, shown in Fig. 11c,d. After 4 min of Vis light irradiation, there are significant differences on the two free radicals of TiO_2, β-$NaYF_4$:Ho^{3+}@TiO_2, and β-$NaYF_4$:Ho^{3+}@TiO_2-rGO. As for TiO_2, the Vis light is not enough to excite TiO_2, so that the signals of both free radicals can hardly be detected. Since β-$NaYF_4$:Ho^{3+}@TiO_2 is capable of converting Vis light into UV light, and excite TiO_2 to result separation of electron-hole pairs, it can detect strong signals of ·OH and $\cdot O_2^-$. After introducing rGO, i.e. in β-$NaYF_4$:Ho^{3+}@TiO_2-rGO system, the signals of both radicals are significantly increased, wherein the signals of ·OH and $\cdot O_2^-$ are 3.2-fold and 2.1-fold of those in β-$NaYF_4$:Ho^{3+}@TiO_2 system. This result indicates that β-$NaYF_4$:Ho^{3+}@TiO_2-rGO can generate more free radicals to take part in photocatalytic reaction, so as to improve the photocatalytic activity. Owe to the super conductive performance of rGO, larger amounts of free radicals can be produced, which can effectively separate electron-hole pairs and extend the lifetime of charge carrier.

3D fluorescence spectra. Photoluminescence (PL) spectra reflect the migration, transfer, and recombination processes of the electronhole pairs[73,74]. Figure 12 shows 3D fluorescence spectra β-$NaYF_4$:Ho^{3+}, β-$NaYF_4$:Ho^{3+}@TiO_2, and β-$NaYF_4$:Ho^{3+}@TiO_2-rGO composite. The plots show that UC and catalysts have a maximum fluorescence peak near (λ_{ex}, λ_{em}) = (205 nm, 315 nm(335 nm)), (λ_{ex}, λ_{em}) = (240 nm, 315 nm), and (λ_{ex}, λ_{em}) = (205 nm, 315 nm), which is attributed to the recombination of holes and electrons across the band gap of β-$NaYF_4$:Ho^{3+}. The β-$NaYF_4$:Ho^{3+}@TiO_2 composites absorb slightly weakly than β-$NaYF_4$:Ho^{3+}, which implies that the recombination of photogenerated electrons and holes is less in the β-$NaYF_4$:Ho^{3+}@TiO_2 composites. The β-$NaYF_4$:Ho^{3+}@TiO_2-rGO composites absorb more weakly than β-$NaYF_4$:Ho^{3+} and β-$NaYF_4$:Ho^{3+}@TiO_2,

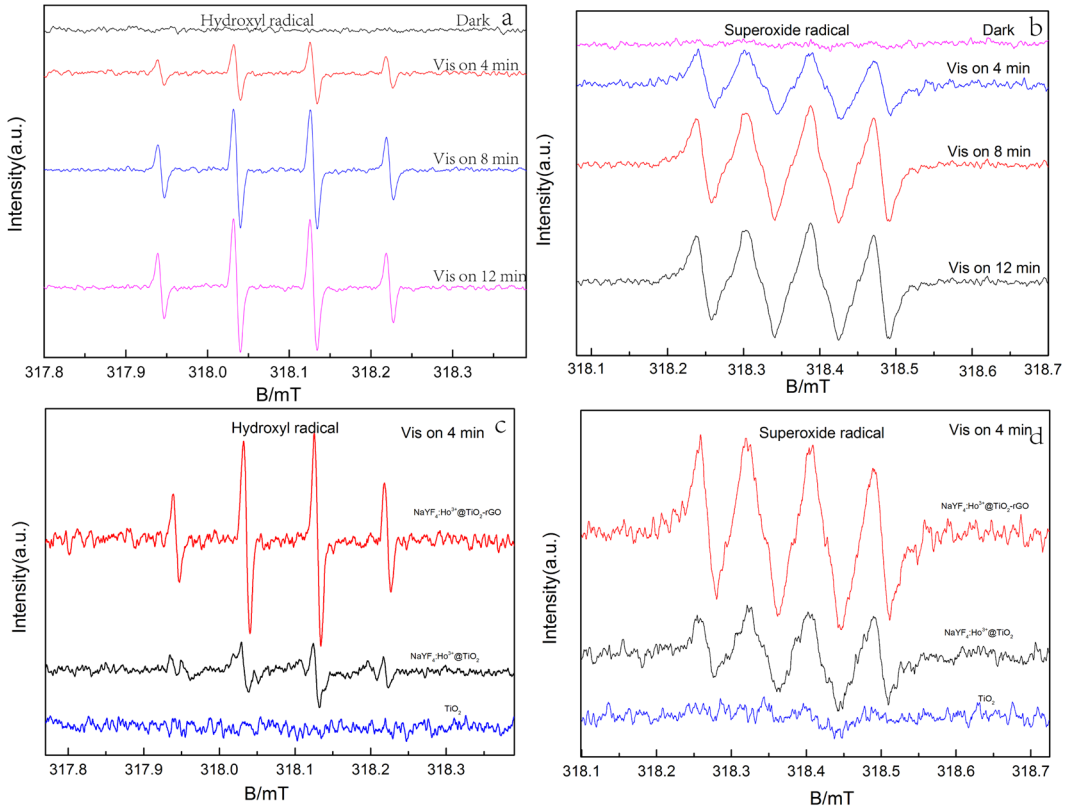

Figure 11. DMPO spin-trapping ESR spectra of β-NaYF4:Ho^{3+}@TiO2-rGO in methanol dispersion for OH (**a**) and in aqueous dispersion for·$O2^{-}$ (**b**); (**c**) superoxide radical, (**d**) hydroxyl radicals of TiO2, β-NaYF4:Ho^{3+}, and β-NaYF4:Ho^{3+}@TiO2-rGO after four min of Vis light irradiation.

which implies that the recombination of photogenerated electrons and holes is much less in the β-$NaYF_4$:Ho^{3+}@TiO_2-rGO. The results above are consistent with Photoelectrochemical measurements analysis results.

A possible reaction process is proposed in Figure. 13, which can be summarized in the equations below. The β-$NaYF_4$:Ho^{3+}UC absorbs visible light and emits UV light (R1). The detailed process can be described as below. First Ho^{3+} jumps from ground state $^5I_8$ energy level to excited state $^5F_1$ ($^5I_8 \rightarrow {}^5F_1$) energy level via Ground State Absorption (GSA) under the excitation of 450 nm light source, meanwhile it jumps via nonradiative cross relaxation back to excited state $^5I_4$ energy level ($^5F_1 \rightarrow {}^5I_4$), rather than back to excited state $^5I_6$ energy level. In the second stage, the Ho^{3+}, which locates on excited state $^5I_4$ energy level, absorbs the photon of the same energy, and then directly jumps via ESA onto excited state $^5D_4$ energy level ($^5I_4 \rightarrow {}^5D_4$). Finally, Ho^{3+} jumps from highly excited level $^5D_4$ back to ground state $^5I_8$ ($^5D_4 \rightarrow {}^5I_8$), while emitting 288 nm UV light, so that the two-photon UC luminescence mechanism is completed. Through UV excitation, electron-hole pairs are generated on the TiO_2 surface (R2), which is followed by rapid transfer of photogenerated electrons to rGO sheets via percolation mechanism (R4). The excited electrons on the TiO_2 surface react with the absorbed oxygen, resulting in the formation of $\cdot O_2^-$ or $HO_2\cdot$. After that, it can form hydrogen peroxide (H_2O_2; R5) through combining H^+ with $\cdot O_2^-$ or $HO_2\cdot$. H_2O_2 reacts with the superoxide radical anion ($\cdot O_2^-$), and then reduces it into a hydroxyl radical (·OH; R7). The photogenerated holes react with H_2O, resulting in the formation of hydroxyl radicals (·OH; R3). The conduction band of TiO_2 is located above the RhB redox potential, which allows TiO_2 to be catalytically active. Therefore, these reactive oxygen species (i.e., ·OH, $\cdot O_2^-$, and H_2O_2), especially ·OH, can oxidize the organic molecules and perform photocatalysis (R7). The entire sequence is summarized as below:

$$NaYF_4{:}\ Ho^{3+} + \text{visible light} \rightarrow NaYF_4{:}\ Ho^{3+} + UV \quad (1)$$

$$TiO_2 + UV \rightarrow TiO_2(h^+ + e^-) \quad (2)$$

$$H_2O + TiO_2(h^+) \rightarrow \cdot OH + H^+ \quad (3)$$

$$TiO_2(e^-) + rGO \rightarrow TiO_2 + rGO\,(e^-) \quad (4)$$

$$O_2 + H^+ + rGO(e^-) \rightarrow \cdot O_2^- + H_2O_2 \quad (5)$$

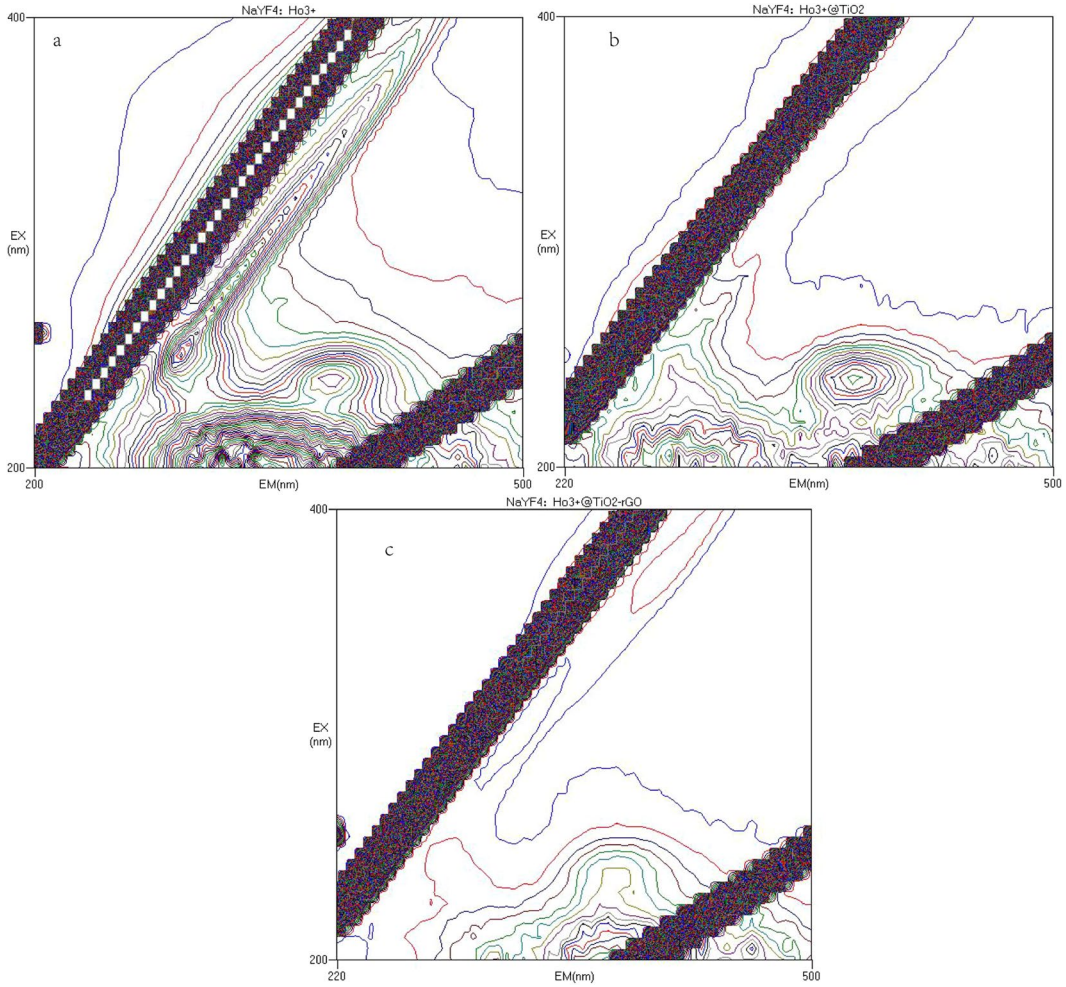

Figure 12. 3D fluorescence spectra of NaYF4:Ho^{3+} (**a**), NaYF4:Ho^{3+}@TiO2 (**b**), and NaYF4:Ho^{3+}@TiO2-rGO composite (**c**).

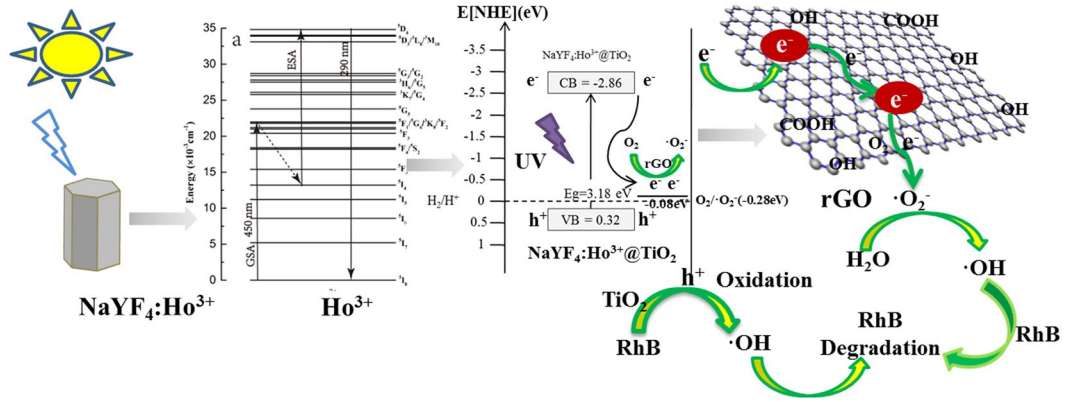

Figure 13. Photocatalytic reaction mechanism of β-NaYF4:Ho^{3+}@TiO2-rGO.

$$\cdot O_2^- + H_2O_2 \rightarrow \cdot OH + OH^- + O_2 \quad (6)$$

$$\cdot OH\,(\text{or } \cdot O_2^-) + \text{RhB} \rightarrow \text{degradation products} \quad (7)$$

Conclusions

In summary, we have successfully prepared β-$NaYF_4$:Ho^{3+}@TiO_2-rGO composites as an advanced Vis-driven photocatalyst by using a simple hydrothermal method. We demonstrated a new strategy by integrating the Vis-to-UV UC property of β-$NaYF_4$:Ho^{3+} with the excellent electrical properties of GR to enhance the photocatalytic efficiency of TiO_2. Photocatalytic properties of the β-$NaYF_4$:Ho^{3+}@TiO_2-rGO composites were evaluated by the degradation of an RhB solution. The enhanced photocatalytic activity was associated with the large extended photoresponsive range, great adsorptivity of dyes and high electron–hole separation efficiency due to the synergetic interactions among TiO_2, GR and UC material. This work is expected to promote practical applications of photocatalysts under solar irradiation in the hope of addressing various environmental issues.

Experimental Section

Materials and reagents. All chemicals were used as received without further purification. Y_2O_3 (99.999% purity), Ho_2O_3(>99.9% purity) and GO solution(>99.85% purity) were of high purity. All other chemicals, including NaF, ethanol, ethylenediaminetetraacetic acid (EDTA), tetra-n-butyl titanate (TBOT), and polyvinylpyrrolidone K-30 (PVP) were in analytical grade. Y_2O_3, NaF, TBOT, and PVP were purchased from Chengdu Kelong Chemical Co. Ltd. (Sichuan, China). Ho_2O_3 was obtained from Shanghai Tongna Environmental Protection Co. Ltd. (China). EDTA was purchased from Chongqing Boyi Chemical Co. Ltd. (China). HNO_3 and ethanol were obtained from Chongqing Chuandong Chemical Group Co. Ltd. (China).GO solutionwas obtained from Shanghai HuaYiCo. Ltd. (China).

Synthesis of $NaYF_4$:Ho^{3+}@TiO_2–rGOternarycomposites. The $NaYF_4$:Ho^{3+}@TiO_2 core-shell microcrystals were synthesized by referring preliminary work[35]. UV-irradiation of the$NaYF_4$:Ho^{3+}@TiO_2-graphene oxide samples was performed using a hydrothermal method. Firstly, 2 mg/mL GO (2.5 mL) was ultrasonicated in 100 mL of anhydrous ethanol solution till being well dispersed; after that, 0.1 g of $NaYF_4$:Ho^{3+}@$TiO_2$was added into the above GO solution and then keep vigorous stirring for 1 h. The resulting mixture was transferred into a 100 mL stainless Teflon-lined autoclave filled with deionized water up to 80% of its capacity. The autoclave was tightly sealed and heated at 130 °C for 4 h, after that the system was allowed to cool to room temperature naturally. The precipitate was centrifuged and washed with deionized water for two times and then dried in the vacuum freeze drier at −60 °C for 24 h, before resulting in $NaYF_4$:Ho^{3+}@TiO_2-rGO composites.

Photocatalytic activity measurement. The photocatalytic activity of the $NaYF_4$:Ho^{3+}@TiO_2-rGO composites was measured via comparing the concentration of rhodamine B (RhB) after irradiation to the original concentration of RhB using a Hitachi U-3010 UV-Vis spectrophotometer (Hitachi Corp., Tokyo, Japan). The percentage of degradation is indicated as C/C_0, where C is the concentration of RhB at the irradiation time t and C_0 is the concentration at adsorption equilibrium with the photocatalyst before irradiation. Typically, 50 mg of photocatalyst was suspended in 250 mL RhB aqueous solution (5 mg/L) by sonication. Prior to irradiation, the suspension was stirred in the dark for 0.5 h to establish the adsorption-desorption equilibrium. Then the solution was exposed to the irradiation of a500 W Xenon arc lamp with a UV cutoff filter ($\lambda > 400$ nm). Every 2 hour, 8 mL of the transparent, aqueous solution was collected and then centrifuged (10,000 r/min) prior to analysis with the Hitachi U-3010 UV-Vis spectrophotometer. As reference experiments, t the photodegradation of RhB with P25 (Degussa P25), with β-$NaYF_4$:Ho^{3+}, and without any catalyst were tested, respectively. All the experiments were at the same conditions for comparison.

Characterization. The crystal structures of all prepared samples were characterized by X-ray diffraction (XRD) using a Rigaku D/Max2500pc diffractometer with Cu Kα radiation. Scanning electron microscopy (SEM) images were obtained with a Zeiss AURIGA FE microscope (EHT = 5 kV, WD = 8.8 nm; Zeiss, Oberkochen, Germany). An energy-dispersive X-ray analysis (EDS) of the samples was also performed during the SEM measurements. Transmission electron microscopy (TEM) measurements were carried out on a FEI Tecnai G20 operated at an acceleration voltage of 200 kV. The surface chemical environments were analyzed by X-ray photoelectron spectra (XPS) on a PHI5000 VersaProbe system with monochromatic Al Kα X-rays. The composite was applied with Fourier transform infrared spectroscopy analysis (FT-IR, IRPrestige-21, Shimadzu, Japan) using FT-IR spectrophotometer (KBr as the reference sample). UV-Vis diffuse-reflectance spectroscopy (UV-Vis DRS) was performed using the Hitachi U-3010 UV-Vis spectrophotometer. Raman spectra were recorded on an HR Evolution instrument with an Ar + laser source of 488 nm. The Brunauer-Emmett-Teller (BET) surface areas measurements and evaluation of porosity of the samples were conducted on the basis of nitrogen adsorption isotherms measured at 400 °C using a gas adsorption apparatus (Gemini VII 2390, Micromeritics Instrument Corp, Norcross, GA, USA). The sample for electron spin resonance (ESR) measurement was prepared by mixing $NaYF_4$:Ho^{3+}@TO–rGO samples in a 50 mM DMPO solution tank (aqueous dispersion for DMPO-·OH and methanol dispersion for DMPO-·O_2^-). Photoelectrochemical properties were evaluated using CHI Electrochemical Workstation (CHI 760E, Shanghai Chenhua, China). All the photoelectrochemical measurements were performed under Vis light of a 300 W Xe lamp coupled with 420 nmcutoff filters. Three-dimensional (3D) fluorescence spectra were obtained with a Hitachi F-7000 fluorescence spectrophotometer with a 150 W Xe lamp as excitation source. All experiments were performed at room temperature.

References

1. Honda, A. *et al.* Electrochemical Photolysis of water at a semiconductor electrode. *Nature.* **238**, 37–38 (1972).
2. Reddy, K. R., Hassan, M. & Gomes, V. G. Hybrid nanostructures based on titanium dioxide for enhanced photocatalysis. *ApplCatal A.* **489**, 1–16 (2015).
3. Fujishima, K. H. *et al.* TiO_2 Photocatalysis: A Historical Overview and Future Prospects. Jpn. J. *Appl. Phys.* **44**, 8269–8285 (2005).

4. Kumar, S. G. & Devi, L. G. *et al*. Review on Modified TiO_2 Photocatalysis under UV/Visible Light: Selected Results and Related Mechanisms on Interfacial Charge Carrier Transfer Dynamics. *J.Phys. Chem. A*. **115**, 13211–13241 (2011).
5. Hassan, K. R. *et al*. Carbon Functionalized TiO_2 Nanofibers for High Efficiency Photocatalysis. Mater. *Res. Exp.* **1**, 12–15 (2014).
6. Wen, J., Li, X. & Liu, W. *et al*. Photocatalysis fundamentals and surface modification of TiO_2, nanomaterials[J]. *Chinese J Cata* **36**, 2049–2070 (2015).
7. Wonyong, C., Andreas, T. & Hoffmann, M. R. Effects of Metal-Ion Dopants on the Photocatalytic Reactivity of Quantum-Sized TiO_2 Particles. *Angew. Chem. Int. Ed.* **33**, 1091–1092 (1994).
8. Tang, Y. *et al*. NIR-Responsive Photocatalytic Activity and Mechanism of $NaYF_4$:Yb,Tm@TiO_2 CoreS-hell Nanoparticles. *ACS Catal.* **3**, 405–412 (2013).
9. Kaur, N. Strategies for modification of titania to harness visible light-A review. *Catal.eprints.iitm.ac.in.* **25**, 26–38 (2014).
10. Liu, J. T. *et al*. Recent progress in design, synthesis, and applications of one-dimensional TiO_2 nanostructured surface heterostructures_ a review. *Chem. Soc. Rev.* **43**, 6920–6937 (2014).
11. Luan, J. C. *et al*. Constructing Hierarchical Spheres From Large Ultrathin Anatase TiO_2 Nanosheets With Nearly 100% Exposed (001) Facets for Fast Reversible Lithium Storage. *J.Am. Chem. Soc.* **28**, 6124–6130 (2016).
12. Jinfeng, Z., Yunguang, Y. & Wei, L. Preparation, Characterization, and Activity Evaluation of CuO/F-TiO_2 Photocatalyst. *Int. J. Photoenergy.* **2012**, 1–9 (2012).
13. Wei Seh, Z. *et al*. Sulphur–TiO_2 yolk–shell nanoarchitecture with internal void space for long-cycle lithium–sulphur batteries. *Nature Comm.* **4**, 1331–1338 (2013).
14. Liu, Z. S. *et al*. Janus Au-TiO_2 Photocatalysts with Strong Localization of Plasmonic Near-Fields for Efficient Visible-Light Hydrogen Generation. *Adv Mater.* **24**, 2310–2314 (2012).
15. Lu, M. *et al*. p-MoO_3 Nanostructures/n-TiO_2 Nanofiber Heterojunctions: Controlled Fabrication and Enhanced Photocatalytic Properties. *Appl. Mater. Int.* **6**, 9004–9012 (2014).
16. Makarova, O. V. *et al*. Surface Modification of TiO_2 Nanoparticles For Photochemical Reduction of Nitrobenzene. *Environ. Sci. Technol.* **34**, 4797–4803 (2000).
17. Zhou, J. *et al*. TiO_2 nanotubes: Structure optimization for solar cells. *J. Mater. Chem.* **21**, 9406–9418 (2011).
18. Han, W., Wang, Y. & Zheng, Y. *In Vitro* Biocompatibility Study of Nano TiO_2 Materials. *Adv. Mater. Res.* **47**, 1438–1441 (2008).
19. Schlick, T. *et al*. Molecular dynamics-based approaches for enhanced sampling of long-time, large-scale conformational changes in biomolecules. *Biol Rep.* **1**, 51–57 (2009).
20. Srivastava, N. & Tiwari, T. New trends in polymer electrolytes: a review. *e-Polymers.* **9**, 1–18 (2009).
21. Ding, M. *et al*. Simultaneous morphology manipulation and upconversion luminescence enhancement of β-$NaYF_4$:Yb^{3+}/Er^{3+} microcrystals by simply tuning the KF dosage. *Sci Rep.* **5**, 12745–12759 (2015).
22. Lu, D. *et al*. Experimental demonstration of plasmon enhanced energy transfer rate in $NaYF_4$:Yb^{3+}/Er^{3+} upconversion nanoparticles. *Sci Rep.* **6**, 18894–18905 (2016).
23. Wang, G. *et al*. Size-dependent upconversion luminescence in YF_3:Yb^{3+}/Tm^{3+} nanobundles. *J. Fluorine Chem.* **129**, 1110–1113 (2008).
24. Lerouge, G. J. *et al*. Real-time, non-invasive monitoring of hydrogel degradation using $LiYF_4$:Yb^{3+}/Tm^{3+} NIR-to-NIR upconverting nanoparticles. *Nanoscale.* **7**, 11255–11262 (2015).
25. Guo, X. *et al*. Preparation and upconversion luminescence of beta-$NaYF_4$:Yb^{3+}, Tm^{3+}/ZnO nanoparticles. *J.Nano.Nanotechnol.* **14**, 3726–3730 (2014).
26. Guo, X. *et al*. Enhanced near-infrared photocatalysis of $NaYF_4$:Yb,Tm/CdS/TiO_2 composites. *Dalton Trans.* **43**, 1048–1054 (2014).
27. Zhang, Y. & Hong, Z. Synthesis of lanthanide-doped $NaYF_4$@TiO_2 core–shell composites with highly crystalline and tunable TiO_2 shells under mild conditions and their upconversion-based photocatalysis. *Nanoscale.* **5**, 8930–8933 (2013).
28. Wang, W. *et al*. Different Upconversion Properties of β-$NaYF_4$:Yb^{3+},Tm^{3+}/Er^{3+} in Affecting the Near-Infrared-Driven Photocatalytic Activity of High-Reactive TiO_2. *Appl. Mater. Int.* **6**, 340–348 (2014).
29. Wu, X. *et al*. UV, visible and near-infrared lights induced NO_x destruction activity of (Yb,Er)-$NaYF_4$/C-TiO_2 composite. *Sci Rep.* **3**, 2918–2925 (2013).
30. Wang, W. *et al*. A study on upconversion UV-vis-NIR responsive photocatalytic activity and mechanisms of hexagonal phase $NaYF_4$:Yb^{3+},Tm^{3+}@TiO_2 core-shell structured photocatalyst. *Appl. Catal., B.* **144**, 379–385 (2014).
31. Qin, W. *et al*. Near-infrared photocatalysis based on YF_3:Yb^{3+},Tm^{3+}/TiO_2 core/shell nanoparticles. *Chem Comm.* **46**, 2304–2312 (2010).
32. Ye, Q. *et al*. Synthesis of UV/NIR photocatalysts by coating TiO_2 shell on peanut-like YF_3:Yb,Tm upconversionnanocrystals. *Mater Lett.* **106**, 238–241 (2013).
33. Li, T. *et al*. Ultraviolet upconversion luminescence in Y_2O_3:Yb^{3+},Tm^{3+} nanocrystals and its application in photocatalysis. *J. Mate. Sci.* **46**, 2882–2886 (2011).
34. Tsuboi, T. *et al*. Optical spectroscopy of heavily Ho^{3+}-doped BaY_2F_8 crystals. *J. Lumin.* **131**, 695–700 (2011).
35. Wu, T. H. & Long, J. *et al*. Synthesis and Photocatalytic Activity of Hexagonal Phase $NaYF_4$:Ho^{3+}@TiO_2 Core-Shell Microcrystals. *CrystEngComm* **18**, 6471–6482 (2016).
36. Ren, L. *et al*. Upconversion-P25-graphene composite as an advanced sunlight driven photocatalytic hybrid material. *J. Mater. Chem.* **22**, 11765–11770 (2012).
37. Allen, M. J., Tung, V. C. & Kaner, R. B. Honeycomb Carbon: A Review of Graphene. *Chem Rev.* **110**, 132–145 (2010).
38. Imoto, K. *et al*. A weak-value model for virtual particles supplying the electric current in graphene the minimal conductivity and the Schwinger mechanism. *New J. Phys.* **16**, 264–571 (2014).
39. Li, X., Yu, J. & Wageh, S. *et al*. Graphene in Photocatalysis: A Review[J]. *Small* **12**, 6640 (2016).
40. Miao, J., Xie, A. & Li, S. *et al*. A novel reducing graphene/polyaniline/cuprous oxide composite hydrogel with unexpected photocatalytic activity for the degradation of Congo red [J]. *Appl. Surf. Sci* **360**, 594–600 (2016).
41. Wang, D. *et al*. Self-Assembled TiO_2-Graphene Hybrid Nanostructures for Enhanced Li-Ion Insertion. *ACS Nano* **3**, 907–914 (2009).
42. Lv, X., Zhang, G. & Fu, W. Highly Efficient Hydrogen Evolution Using TiO_2/Graphene Composite Photocatalysts. *Protein Eng.* **27**, 570–576 (2012).
43. Zhang, Y. & Pan, C. TiO_2/Graphene Composite from Thermal Reaction of Graphene Oxide and its Photocatalytic Activity in Visible Light. *J Mater Sci.* **46**, 2622–2626 (2011).
44. Yadav, P. *et al*. Probing the electrochemical properties of TiO_2/graphene composite by cyclic voltammetry and impedance spectroscopy. *Mater. Sci. Eng., B.* **206**, 22–29 (2016).
45. Xiang, Q., Cheng, B. & Yu, J. Graphene-Based Photocatalysts for Solar-Fuel Generation[J]. *Angew. Chem. Int. Edit.* **54**, 11350 (2015).
46. Hu, X. Y., Zhou, K. & Chen, B. Y. *et al*. Graphene/TiO_2/ZSM-5 composites synthesized by mixture design were used for photocatalytic degradation of oxytetracycline under visible light: Mechanism and biotoxicity[J]. *Appl. Surf.Sci* **362**, 329–334 (2016).
47. Huang, M., Yu, J. & Hu, Q. *et al*. Preparation and enhanced photocatalytic activity of carbon nitride/titania(001 vs 101 facets)/reduced graphene oxide (g-C_3N_4/TiO_2/rGO) hybrids under visible light[J]. *Appl. Surf. Sci* **389**, 1084–1093 (2016).
48. Pham, T. T., Nguyen-Huy, C. & Shin, E. W. Facile one-pot synthesis of nickel-incorporated titanium dioxide/graphene oxide composites: Enhancement of photodegradation under visible-irradiation[J]. *Appl. Surf. Sci* **377**, 301–310 (2016).
49. Song, Q. H. *et al*. Enhanced Photocatalytic Activity of Chemically Bonded TiO_2/Graphene Composites Based on the Effective Interfacial Charge Transfer through the C–Ti Bond. *Acs. Catal.* **3**, 1477–1485 (2013).

50. Cui, G. L. *et al*. Highly dispersive nano-TiO_2 *in situ* growing on functional graphene with high photocatalytic activity. *J. Nano. Res.* **18**, 1–8 (2016).
51. Wang, W. *et al*. Graphene supported β-$NaYF_4$:Yb^{3+},Tm^{3+} and N doped P25 nanocomposite as an advanced NIR and sunlight driven upconversionphotocatalyst. *Appl. Surf. Sci.* **282**, 832–837 (2013).
52. Wang, W. *et al*. A NIR-driven photocatalyst based on α-$NaYF_4$:Yb,Tm@TiO_2 core–shell structure supported on reduced graphene oxide. *Appl. Catal B* **182**, 184–192 (2016).
53. Zeng, J. H. *et al*. Synthesis and Upconversion Luminescence of Hexagonal-Phase $NaYF_4$:Yb, Er^{3+} Phosphors of Controlled Size and Morphology. *Adv. Mater.* **17**, 2119–2123 (2005).
54. Yin, B. J. Q. Z. Synthesis, crystallinity control, and photocatalysis of nanostructured titanium dioxide shells. *J. Mater. Res.* **28**, 362–368 (2013).
55. Jang, H. K. *et al*. Hierarchical mesoporousanatase TiO_2 nanostructures with efficient photocatalytic and photovoltaic performances. *J. Mater. Chem. A.* **3**, 9714–9721 (2015).
56. Shan, J. & Ju, Y. A single-step synthesis and the kinetic mechanism for monodisperse and hexagonal-phase $NaYF_4$:Yb,Er upconversionnanophosphors. *Nanotechnology.* **20**, 275603–275617 (2009).
57. Xu, Z. *et al*. Harvesting Lost Photons: Plasmon and Upconversion Enhanced Broadband PhotocatalyticActivity in Core@Shell Microspheres Based on Lanthanide-Doped $NaYF_4$, TiO_2, and Au. *Adv. Fun. Mater.* **25**, 2950–2960 (2015).
58. Zhao, Z. L. *et al*. Enhancement of the thermal conductivity of polymer composites with Ag–graphene hybrids as fillers. *Phys. Status Solidi A*. **211**, 2142–2149 (2014).
59. Ye, X. L. *et al*. Fabrication of Highly-Aligned, Conductive, and Strong Graphene Papers Using Ultra large Graphene Oxide Sheets. *AcsNano.* **6**, 10708–10719 (2012).
60. Xu, Y. *et al*. The synergistic effect of graphitic N and pyrrolic N for the enhanced photocatalytic performance of nitrogen-doped graphene/TiO_2 nanocomposites. *Appli.Catal. B.* **181**, 810–817 (2016).
61. Wang, Y. *et al*. Low-temperature solvothermal synthesis of grapheme-TiO_2 nanocomposite and its photocatalytic activity for dye degradation. *Mater Lett.* **134**, 115–118 (2014).
62. Paredes, J. I. *et al*. Graphene Oxide Dispersions in Organic Solvents. *Langmuir* **24**, 10560–10564 (2008).
63. Kai-Chih Hsu, D. H. C. Green synthesis and synergistic catalytic effect of Ag/reduced graphene oxide nanocomposite. *Nanocale ResLett* **9**, 484–488 (2014).
64. Padmanabhan, M. *et al*. Electrochemical Integration of Graphene with Light-Absorbing Copper-BasedThin Films. *J. Phy. Chem. C.* **6**, 1–7 (2012).
65. Du Mao *et al*. Preparation of a Microspherical Silver-Reduced Graphene Oxide-Bismuth Vanadate Composite and Evaluation of Its Photocatalytic Activity. *Materials* **9**, 3–14 (2016).
66. Chen, D. *et al*. Nanospherical like reduced graphene oxide decorated TiO_2 nanoparticles: an advanced catalyst for the hydrogen evolution reaction. *Sci Rep.* **6**, 20335–20339 (2016).
67. Wang, H. & Wang, Y. *et al*. Vibrational properties of graphene and graphene layers. *J Raman Spectrosc* **40**, 1791–1796 (2010).
68. Stankovich, S. *et al*. Synthesis of graphene-based nanosheets via chemical reduction of exfoliated graphite oxide. *Carbon* **45**, 1558–1565 (2007).
69. Leng, W. H. *et al*. Investigation of the Kinetics of a TiO_2 Photoelectrocatalytic Reaction Involving Charge Transfer and Recombination through Surface States by Electrochemical ImpedanceSpectroscopy. *J.Phy. Chem.B.* **109**, 15008–15023 (2005).
70. Natarajan, T. S. *et al*. Study on UV-LED/TiO_2 process for degradation of Rhodamine B dye. *Chem. Eng. J.* **169**, 126–134 (2011).
71. Panpranot, J. *et al*. Synthesis, Characterization, and Catalytic Properties of Pd and Pd-Ag Catalysts Supported on Nanocrystalline TiO_2 Prepared by the Solvothermal Method. *CatalLett* **103**, 53–58 (2005).
72. Lu, P. *et al*. Phosphorus Doping in Si Nanocrystals/SiO_2 msultilayers and Light Emission with Wavelength compatible for Optical Telecommunication. *Sci Rep.* **6**, 22888–22892 (2016).
73. Tang, J. *et al*. Photophysical and photocatalyticproperties of $AgInW_2O_8$. *J Phys. hem B.* **107**, 14265–14269 (2003).
74. Eda, G. *et al*. Blue photoluminescencefrom chemically derived graphene oxide. *Adv. Mater* **22**, 505–509 (2010).

Acknowledgements

Financial support from the Science and Technology Innovation Special Projects of Social Undertakings and Livelihood Support, Chongqing (cstc2016shmszx20009),the Chongqing Research Program of Basic Research and Frontier Technology (cstc2017jcyjB0349), and the 111 Project (B13041)is gratefully acknowledged.

Author Contributions

Z.F. and X.X. designed the experiments. Z.F., X.X. and T.W. performed the experiments and prepared all figures. Z.F. wrote the main manuscript text paper. All authors reviewed the manuscript.

Additional Information

Competing Interests: The authors declare that they have no competing interests.

Publisher's note: Springer Nature remains neutral with regard to jurisdictional claims in published maps and institutional affiliations.